CrossMark

Observed Local Dispersion Relations for Magnetoacoustic-gravity Waves in the Sun's Atmosphere: Mapping the Acoustic Cutoff Frequency

Stuart M. Jefferies[1,2], Bernhard Fleck[3], Neil Murphy[4], and Francesco Berrilli[5]
[1] Georgia State University, 25 Park Place, Atlanta, GA 30303, USA; sjefferies@gsu.edu
[2] University of Hawaii, 34, Ohia Ku Street, Pukalani, HI 96768, USA
[3] ESA Directorate of Science, Operations Department, c/o NASA/GSFC Code 671, Greenbelt, MD 20071, USA
[4] Jet Propulsion Laboratory, Pasadena, CA 91109, USA
[5] Università di Roma Tor Vergata, Via Ricerca Scientifica 1, I-00133 Roma, Italy

Abstract

We present the observed local dispersion relations for magnetoacoustic-gravity waves in the Sun's atmosphere for different levels of magnetic field strength. We model these data with a theoretical local dispersion relation to produce spatial maps of the acoustic cutoff frequency in the Sun's photosphere. These maps have implications for the mechanical heating of the Sun's upper atmosphere, by magnetoacoustic-gravity waves, at different phases of the solar magnetic activity cycle.

Unified Astronomy Thesaurus concepts: Solar oscillations (1515); Solar atmosphere (1477); Solar magnetic fields (1503)

1. Introduction

The mechanisms behind the radiative losses of the atmospheres of stars with outer convection zones, such as the Sun, are still not fully understood (De Moortel & Browning 2015). One mechanism under consideration is mechanical heating by acoustic waves generated by the turbulent convection near the star's surface. When these waves propagate into the star's atmosphere, they can deposit the convective energy they are carrying via shock formation. However, whether or not acoustic waves can propagate in a stratified medium such as a stable atmosphere is determined by the acoustic cutoff frequency of the atmosphere (Lamb 1909). Waves with frequencies below the cutoff frequency are evanescent (i.e., nonpropagating) while waves with frequencies above the cutoff can freely propagate.

Theoretically, the acoustic cutoff frequency approximately scales as $g\sqrt{\mu/T_{\mathrm{eff}}}$ where T_{eff} is the effective temperature, g is the gravity, and μ is the mean molecular weight, with all values measured at the surface. Hence direct measurement of the cutoff frequency can, in principle, be used to constrain the fundamental stellar parameters. Having said that, the acoustic cutoff frequencies for stars (e.g., roAp stars Audard et al. 1998), are currently theoretically determined from stellar models. However, for the Sun we are able to measure the cutoff frequency and we have a mechanism to check our theoretical expectations.

Although the cutoff frequency is expected to be a locally defined quantity (Chae & Litvinenko 2018), only its variation with height has received any attention (Murawski et al. 2016; Wiśniewska et al. 2016; Felipe et al. 2018). To the best of our knowledge, no one has examined how the cutoff frequency varies spatially in latitude and longitude.

2. Observations and Results

For the analysis presented here we used 11 hr of line-of-sight Doppler velocity data acquired on 2017 January 21 from 07:01:30 to 18:01:30 UT using the MOTH II (hereafter referred to as MOTH; Forte et al. 2018) and *SDO*/HMI (Scherrer et al.

2012; Schou et al. 2012) instruments. In addition, to probe the lower photosphere, we also used 11 hr of Doppler velocities derived from the first and second Fourier coefficients calculated from the individual HMI filtergrams (Couvidat et al. 2012; Nagashima et al. 2014) acquired on 2010 August 24 from 00:00:00 to 11:00:00 UT (i.e., during solar minimum conditions). The Doppler signal derived from the phase of the second Fourier coefficients is closer to a line core Doppler signal than the standard HMI Doppler signal, which is derived from the phase of the first Fourier coefficients. Applying the procedure of Fleck et al. (2011) to the Doppler signal derived from the second Fourier coefficients suggests a formation height that is about 40 km higher than that of the standard HMI Doppler velocities, i.e., at around 180 km versus 140 km (taking into account the limited spatial resolution, which shifts the apparent line formation by about 40–50 km to larger heights).

The MOTH II instruments use the Na 589 nm and K 770 nm solar absorption lines to sample the upper photosphere/lower chromosphere region of the Sun's atmosphere, while the HMI instrument uses the Fe 617 nm line to sample the lower photosphere. The MOTH II observations were acquired at a cadence of 5 s but were integrated to a 45 s cadence to be commensurate with the HMI sampling rate. Both the MOTH II and the HMI data were spatially binned to yield an effective pixel size of 1″27.

We computed the cross-power spectra $\mathrm{CP}(\omega) = F_{V_1}(\omega) \cdot F_{V_2}(\omega)^\star$ with F denoting the Fourier transform of the measured velocity signals V_1 and V_2 between the 2017 MOTH and HMI data sets (i.e., Na–Fe, K–Fe, and Na–K) and between the two 2010 HMI data sets (i.e., Fe–Fe) for each spatial pixel in a $1060'' \times 1060''$ region near disk center. For the 2010 HMI data sets we used a smaller region of $518'' \times 518''$ (center 1024 × 1024 pixels of the full 4k × 4k resolution HMI Dopplergrams). We then averaged the cross-power spectra over different ranges of magnetic field strength and calculated the phase difference spectra $\Delta\phi(\omega) = \arctan(\mathrm{Imaginary}(\mathrm{CP}(\omega))/\mathrm{Real}(\mathrm{CP}(\omega))$ to provide the curves shown in Figure 1.
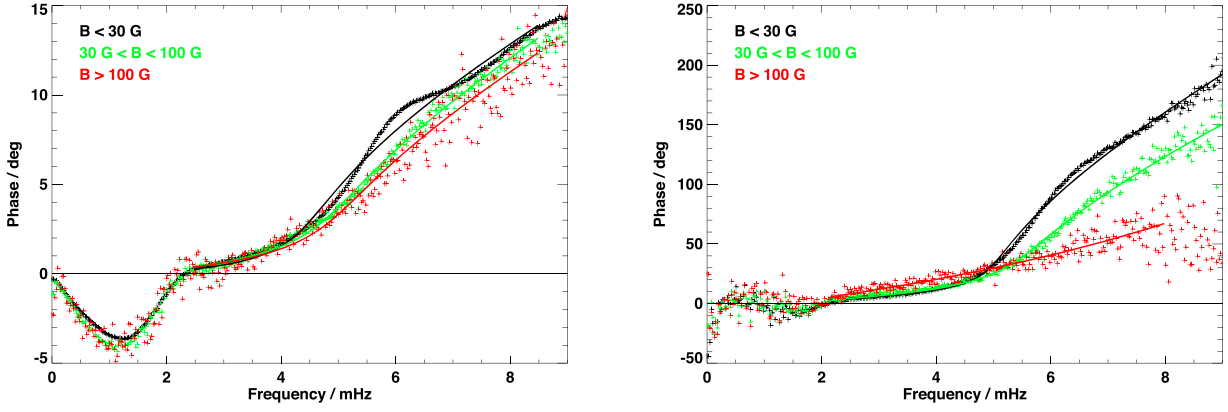
Figure 1. Observed phase differences (denoted by crosses) in three different regions of magnetic field strength, $|B| \leqslant 30$ G (black), 30 G $< |B| \leqslant 100$ G (green), and $|B| > 100$ G (red), and at two different heights in the Sun's photosphere. In this Letter we consider the phase differences above 2 mHz. Fits using Equations (2) and (3) are overlaid (thick solid lines). The phase difference spectra for the 2010 Fe–Fe observations (lower photosphere) are shown on the left and represent the mean of 977,253, 64,599, and 6764 individual phase difference spectra for the black, green, and red data, respectively. The phase difference spectra for the 2017 Na–Fe observations (upper photosphere) are shown on the right and represent the mean of 616,630, 17,298, and 6072 individual phase difference spectra for the black, green, and red data, respectively.

To model the observed phase difference we start by defining the vertical component of the velocity induced by a upward propagating plane wave of angular frequency ω and angular wave number $\boldsymbol{k}$, where $k^2 = k_x^2 + k_z^2$, k_x and k_z are the horizontal and vertical components, respectively, as the real part of

$$v_z(x, z, t) = U_z(0) \exp \kappa z \exp \left[i(\omega t - k_z z - k_x x) \right], \quad (1)$$

where $U_z(0)$ is the amplitude of the wave at height $z = 0$ and κ is related to the scale height of the atmosphere (see below). The phase difference $\Delta \phi$ is given by

$$\Delta \phi = k_z \Delta z = \omega \Delta t_{\mathrm{ph}}, \quad (2)$$

where Δz is the height difference $(z_2 - z_1)$ between the observations and Δt_{ph} is the phase travel time of the wave between the observations. Equation (2) shows that the observed variation of $\Delta \phi$ with frequency provides a measure of the local magnetoacoustic-gravity wave dispersion relation for upward propagating waves.

We define the magnetically quiet Sun as being the spatial locations where the unsigned line-of-sight magnetic flux from HMI $|B| < 30$ G, and model the corresponding measured phase difference spectra, above 2 mHz, using Equation (2) and k_z as defined by the dispersion relation for acoustic-gravity waves in an isothermal stratified atmosphere with constant radiative damping (Souffrin 1972), i.e.,

$$k_z = \pm \left[\frac{a}{2} + \frac{\sqrt{a^2 + b^2}}{2} \right]^{\frac{1}{2}} \quad (3)$$

$$\kappa = \left(\frac{1}{2H} \right) - \left[\frac{-a}{2} + \frac{\sqrt{a^2 + b^2}}{2} \right]^{\frac{1}{2}}, \quad (4)$$

where

$$a = \frac{\omega^2 - \omega_{\mathrm{ac}}^2}{c_s^2} + k_x^2 \left(\frac{N^2}{\omega^2} - 1 \right) - \frac{1}{1 + \omega^2 \tau_R^2} \frac{N^2}{\omega^2} \left(k_x^2 - \frac{\omega^4}{g^2} \right) \quad (5)$$

and

$$b = \frac{\omega \tau_R}{1 + \omega^2 \tau_R^2} \left(\frac{N^2}{\omega^2} \right) \left(k_x^2 - \frac{\omega^4}{g^2} \right). \quad (6)$$

Here ω_{ac} is the acoustic cutoff frequency, N is the buoyancy frequency, τ_R is the radiative damping time, c_s is the local sound speed, γ is the adiabatic exponent, and g is the acceleration due to gravity.

The variables in the model are $(c_s, \Delta z, \omega_{\mathrm{ac}}, \tau_R)$, and the buoyancy frequency is obtained through the identity

$$N = (\gamma - 1)^{\frac{1}{2}} g / c_s. \quad (7)$$

In the photosphere $g = 274$ m s^{-2} and γ is taken to be 5/3. We set $k_x = 0$ so as to only consider vertically propagating waves.

The results are shown in Figure 1. As can be seen in both panels of this figure the theoretical phase difference curve generated using Equations (2) and (3)) models the overall behavior of the observed phase difference data well. However, it does not display sufficient flexibility to model the small "wave" in the observed phase difference spectra that is centered just above 6 mHz. (We note that we also see the same behavior in a MOTH K–HMI Fe phase difference plot, which is not shown here because of space limitations.) There is clearly some physics that is not being addressed in Equation (2). To address this we turn to the observed spatial maps of power at high frequencies (>5 mHz), for the MOTH II Na and HMI data sets (see Figure 2).

The behavior in these maps has been well described by the recent modeling of Rijs et al. (2015) who showed that the "halos" of increased power near active regions is caused by waves reflected from the region where the Alfvén speed, a, is commensurate with the sound speed, c_s. Basically, fast acoustic waves with frequencies above the acoustic cutoff frequency propagate up to the $a = c_s$ layer, where they are transmitted and converted into slow acoustic waves and fast magnetic waves, respectively. The slow acoustic waves continue their journey upward, guided by the magnetic field lines. The fast magnetic waves, however, are refracted and then finally reflected at the height where $\omega / k_x = a$ is met (Rijs et al. 2015). These reflected waves then transmit and convert into slow magnetic and fast acoustic waves, respectively. The
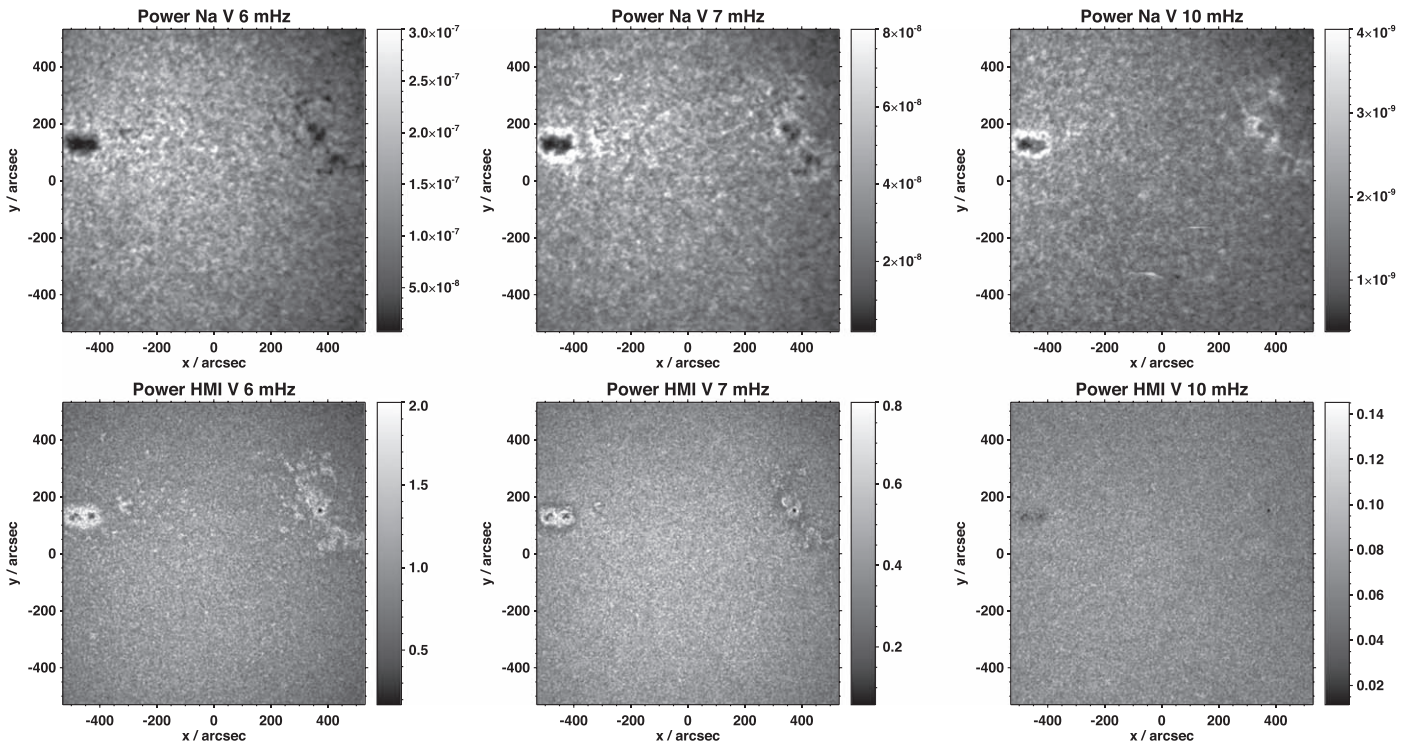
Figure 2. Observed power maps at select frequencies above 5 mHz for the 2017 HMI (bottom row) and MOTH Na observations (top row). The maps at 6 mHz show strong power halos around the magnetic regions in the HMI map but not in the MOTH Na map. The maps at 7 mHz show strong power halos in both the HMI and MOTH Na maps. In addition the HMI map shows regions of suppressed power just outside of the power halos, that is spatially commensurate with the power enhancements seen in the MOTH Na map. Both of these observations are seen in the modeling of Rijs et al. (2015) and point to the existence of downward propagating waves (see also, e.g., Moretti et al. 2007 and Khomenko & Collados 2009).

former are field guided, similar to the slow acoustic waves in the region $a \gg c_s$. Rijs et al. (2015) showed that when wave reflection is suppressed in their model, the power halos disappear. This provides strong evidence that there are downward propagating waves in the solar atmosphere at frequencies above the acoustic cutoff frequency. We note that additional support for the presence of a reflecting layer in the atmosphere is provided in the modulation of the time-distance diagrams for waves with frequencies >5 mHz (Jefferies et al. 1997).

With this in mind, we find that if we model the velocity signal as consisting of upward and downward waves with $k_x = 0$, i.e.,

$$v_z(z, t) = U_z(0)\exp(\kappa z)(\exp[i(\omega t - k_z z)]$$
$$+ \, \alpha \exp[i\psi(\omega)]\exp[i(\omega t + k_z z)]), \qquad (8)$$

where $\alpha \leqslant 1$ is related to the coefficient for the fast acoustic to fast magnetic (and vice versa) wave conversion process, and $\psi(\omega)$ represents a frequency dependent phase change of the wave on reflection (e.g., see Equation (2) of Worrall 1991), then we can produce a "wave" in the observed phase difference spectra that is similar to one we observe. This suggests that accurate modeling of the phase difference spectra should therefore allow for both upward and downward traveling waves.

Now Equation (3) is the dispersion relation for acoustic-gravity waves in an isothermal atmosphere. If we look at the dispersion relations for waves in a magnetic atmosphere, such as Equation (12) in Schunker & Cally (2006), we expect two magnetoacoustic waves that are acoustic-like in their behavior (see Equations (14) and (16) in Schunker & Cally 2006). One is known as the "slow" acoustic wave and it exists above the

$a = c_s$ layer, and the latter is known as the "fast" acoustic wave and it exists below the $a = c_s$ layer. (The "fast" and "slow" waves above and below the $a = c_s$ layer, respectively, are magnetic in character.) For $k_x = 0$, and the two limiting cases $a \gg c_s$ and $c_s \gg a$ we have

$$\omega^2 - \omega_0^2 = c_{\mathrm{ph}}^2 k_z^2, \qquad (9)$$

where $\omega_0 = \omega_{\mathrm{ac}}\eta$ and $c_{\mathrm{ph}} = c_s\eta$ are the modified acoustic cutoff frequency and phase speed, respectively, with $\eta = \cos\theta$ for $a \gg c_s$ and $\eta = 1$ for $c_s \gg a$. Here θ is the inclination angle of the magnetic field to the vertical. In general, η depends on (c_s, a, θ) in a complicated way (Bel & Leroy 1977).

If we neglect the effects of radiative damping, and only consider vertically propagating waves (i.e., $k_x = 0$), then we can see that Equations (3) and (9) have the same form for the dispersion relation. To test if this general model for the dispersion relation can be applied to regions where $a \sim c_s$ we explored the use of Equations (2) and (3) to model the phase difference curves for regions where $|B|$ is larger than our "quiet-Sun" value of 30 G. In this case, however, the parameters associated with c_s and ω_{ac} represent c_{ph} and ω_0. The results, shown by the green and red curves in Figure 1, clearly demonstrate the acoustic-gravity dispersion model works astonishingly well, even for the highest magnetic field strengths.

Since the discrepancies between our theoretical model and the observed phase difference curves are only apparent for the lowest values of magnetic field strength, and even then they are not dramatic, and the individual phase difference spectra for each pixel in our observations are considerably noisier than in the mean spectra, we used Equations (2) and (3) to provide
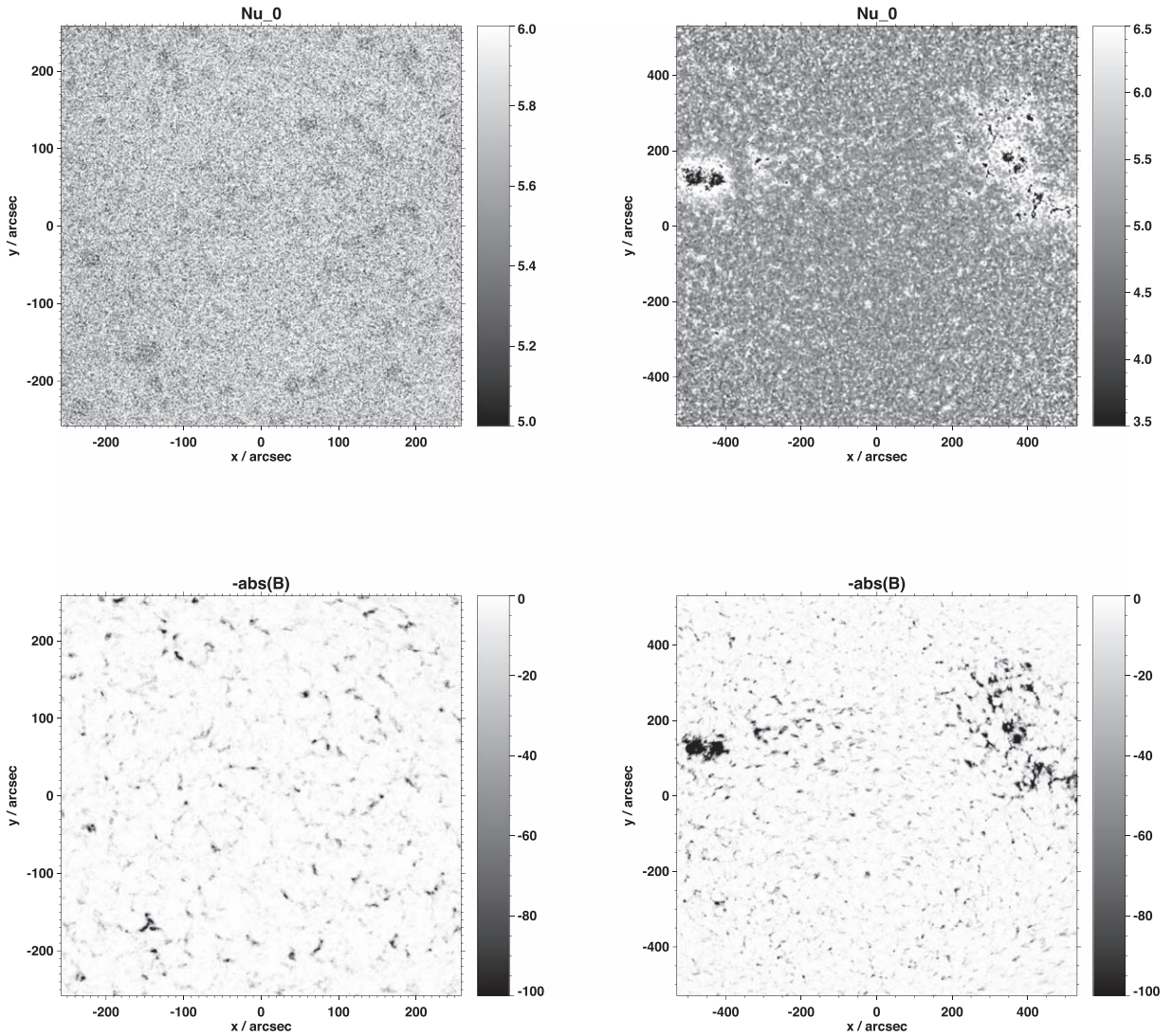
Figure 3. Top row: the modified acoustic cutoff frequency, $\nu_0 = \nu_{ac} \cos\theta = \omega_{ac}/2\pi \cos\theta$ at different heights in the solar atmosphere, in mHz. Left: 2010 Fe–Fe data, i.e., lower photosphere; mean height approximately 160 km. Right: 2017 Na–Fe data, i.e., upper photosphere; mean height approximately 350 km. Bottom row: the average unsigned magnetic field at the height of the HMI observations over the 11 hr observational periods, in G. Left: for the 2010 observations. Right: for the 2017 observations. As expected, the internetwork magnetic field in both magnetograms shows spatial frequencies commensurate with supergranulation scales (the field of view for the Na–Fe data is approximately twice that of the Fe–Fe data). Careful examination of the Fe–Fe cutoff frequency map, which represents the quiet magnetic Sun, shows decreased ν_0 in and around the locations of larger magnetic field. This local reduction in ν_0 is consistent with the presence of magnetoacoustic portals (Jefferies et al. 2006; Rajaguru et al. 2019). These portals allow waves that are normally trapped to escape and propagate in the atmosphere where they can deposit their energy and contribute to the local heating of the atmosphere.

spatial maps of ω_0, c_{ph}, Δz, and τ_R. Because the cross spectra are noisy, we smooth them using a Gaussian of full width at half maximum of 0.5 mHz before we compute the phase difference signal.

Although our analysis provides spatial maps of each of the fitted parameters, in this Letter we focus on the variation of ω_0 in the lower solar atmosphere (see Figure 3). We remind the reader that ω_0 represents a lower limit of ω_{ac}.

We note that while there have been a number of other studies looking at the acoustic cutoff frequency, they have been focused on its variation with height in the atmosphere. Here we are concerned with the spatial variation. We should emphasize, though, that we are not referring to the variation at a fixed geometrical height. The solar atmosphere is highly corrugated and the line contribution functions vary considerably (by several hundred kilometers) over the solar surface (see, e.g., Figures 2 and 3 in Fleck et al. 2011), in particular also in and

around magnetic structures. What we display in Figure 3 are maps of the modified acoustic cutoff frequency between the formation heights of the Doppler signals derived from the Fe and Na lines. Their spatial variations may therefore be a mix of horizontal and vertical variations of the measured quantities. Any study using absorption lines is affected by this effect, and there is no technique that would allow mapping derived physical quantities to a certain, fixed geometrical height.

The maps in Figure 3 show values for $\nu_0 = \omega_0/2\pi$ in magnetic regions that are less than that found in regions of magnetically quiet Sun (defined here as regions where $|B| < 30$ G), surrounded by values of ν_0 that are significantly larger than the quiet-Sun value. The former has been observed before (Felipe et al. 2018); however, to the best of our knowledge, the latter has not. In retrospect, the presence of values of ν_0 larger than the quiet-Sun value was apparent in Figure 3 of Jefferies et al. (2006) where the phase travel-time

curve for the low-β environment (where β is the ratio of gas pressure to magnetic pressure) and small inclination angle is shifted to higher frequencies than the phase travel-time curve for the quiet, "nonmagnetic" Sun.

3. Discussion

The finding of regions in the Sun's atmosphere where the acoustic cutoff frequency is larger than its value in the quiet Sun may provide a connection with other seemingly disparate observations of the Sun's behavior. An increase in the value of ν_{ac} above its value in the quiet Sun would extend the range of frequencies over which waves are trapped beneath the photosphere: it would also cause the effective level of wave reflection for the lower-frequency waves to move inwards. That is, it would result in a shortening of the acoustic cavity. This is because the repulsive properties of the acoustic barrier get stronger (Finsterle et al. 2004). As Finsterle et al. (2004) pointed out, there is some evidence from global helioseismic measurements for such a picture: inversions of the even-splitting rotation coefficients measured from data obtained at different activity levels show the effective acoustic radius of the Sun to be shorter in magnetic regions (Vorontsov 2002), and the acoustic resonance between the excitation source and the upper reflection level, which is sensitive to the acoustic reflectivity of the atmosphere, changes its properties during the solar cycle in a way that is consistent with reflectivity increasing with increasing solar activity (Vorontsov et al. 1998). Indeed, the acoustic cutoff frequency, as measured using low-degree modes, has been shown to increase as solar activity increases (Jiménez et al. 2011). What our results show is how it is increasing.

Basically, the number of regions of increased acoustic cutoff frequency that are present on the Sun will depend on the number of active regions. Therefore, it can be expected that global modes of oscillation will sample a larger region of enhanced cutoff frequency near solar maximum, than at solar minimum.

We note that the ability to measure the spatial variation of the acoustic cutoff frequency has several implications:

I. Compressive waves are one of the proposed mechanisms to explain chromospheric heating (Bello González et al. 2010; Felipe et al. 2011; Kanoh et al. 2016; Krishna Prasad et al. 2017), and a change in acoustic reflectivity will affect the leakage of convective energy into the solar atmosphere. Thus, a detailed characterization of ν_0 is fundamental to estimate which frequencies can actually contribute to the heating.

II. The acoustic cutoff frequency has been shown to be a main contributor to travel-time shift measurements (Lindsey et al. 2010; Schunker et al. 2013; Felipe et al. 2017). Therefore, interpretation of the travel-time shifts will benefit from simultaneous estimations of the atmospheric cutoff frequencies, such as those carried out in this work.

III. The variation of the acoustic cutoff frequency with time has the potential to reveal locations where there are rapid changes in the properties of the atmosphere (i.e., sound speed, strength of the magnetic field, or the angle of inclination of the magnetic field). Such variations might be expected with an eruptive event such as a flare. Tentative evidence for this type of variability was shown by Finsterle et al. (2004). If verified,

maps of acoustic cutoff frequency will provide an important data product for space weather prediction.

ORCID iDs

Francesco Berrilli ⦿ https://orcid.org/0000-0002-2276-3733

References

Audard, N., Kupka, F., Morel, P., Provost, J., & Weiss, W. W. 1998, A&A, 335, 954
Bel, N., & Leroy, B. 1977, A&A, 55, 239
Bello González, N., Flores Soriano, M., Kneer, F., Okunev, O., & Shchukina, N. 2010, A&A, 522, A31
Chae, J., & Litvinenko, Y. E. 2018, ApJ, 869, 36
Couvidat, S., Rajaguru, S. P., Wachter, R., et al. 2012, SoPh, 278, 217
De Moortel, I., & Browning, P. 2015, RSPTA, 373, 20140269
Felipe, T., Braun, D. C., & Birch, A. C. 2017, A&A, 604, A126
Felipe, T., Khomenko, E., & Collados, M. 2011, ApJ, 735, 65
Felipe, T., Kuckein, C., & Thaler, I. 2018, A&A, 617, A39
Finsterle, W., Jefferies, S. M., Cacciani, A., Rapex, P., & McIntosh, S. W. 2004, ApJL, 613, L185
Fleck, B., Couvidat, S., & Straus, T. 2011, SoPh, 271, 27
Forte, R., Jefferies, S. M., Berrilli, F., et al. 2018, in IAU Symp. 335, Space Weather of the Heliosphere: Processes and Forecasts, ed. C. Foullon & O. E. Malandraki (Cambridge: Cambridge Univ. Press), 335
Jefferies, S. M., McIntosh, S. W., Armstrong, J. D., et al. 2006, ApJL, 648, L151
Jefferies, S. M., Osaki, Y., Shibahashi, H., et al. 1997, ApJL, 485, L49
Jiménez, A., García, R. A., & Pallé, P. L. 2011, ApJ, 743, 99
Kanoh, R., Shimizu, T., & Imada, S. 2016, ApJ, 831, 24
Khomenko, E., & Collados, M. 2009, A&A, 506, L5
Krishna Prasad, S., Jess, D. B., Van Doorsselaere, T., et al. 2017, ApJ, 847, 5
Lamb, H. 1909, Proc. London Math. Soc., 7, 122
Lindsey, C., Cally, P. S., & Rempel, M. 2010, ApJ, 719, 1144
Moretti, P. F., Jefferies, S. M., Armstrong, J. D., & McIntosh, S. W. 2007, A&A, 471, 961
Murawski, K., Musielak, Z. E., Konkol, P., & Wiśniewska, A. 2016, ApJ, 827, 37
Nagashima, K., Löptien, B., Gizon, L., et al. 2014, SoPh, 289, 3457
Rajaguru, S. P., Sangeetha, C. R., & Tripathi, D. 2019, ApJ, 871, 155
Rijs, C., Moradi, H., Przybylski, D., & Cally, P. S. 2015, ApJ, 801, 27
Scherrer, P. H., Schou, J., Bush, R. I., et al. 2012, SoPh, 275, 207
Schou, J., Scherrer, P. H., Bush, R. I., et al. 2012, SoPh, 275, 229
Schunker, H., & Cally, P. S. 2006, MNRAS, 372, 551
Schunker, H., Gizon, L., Cameron, R. H., & Birch, A. C. 2013, A&A, 558, A130
Souffrin, P. 1972, A&A, 17, 458
Vorontsov, S. V. 2002, in ESA SP-508, From Solar Min to Max: Half a Solar Cycle with SOHO, ed. A. Wilson (Noordwijk: ESA), 107
Vorontsov, S. V., Jefferies, S. M., Duval, T. L., & Harvey, J. W. 1998, MNRAS, 298, 464
Wiśniewska, A., Musielak, Z. E., Staiger, J., & Roth, M. 2016, ApJL, 819, L23
Worrall, G. 1991, MNRAS, 251, 427